RSC Advances

PAPER

View Article Online
View Journal | View Issue

Check for updates

Cite this: *RSC Adv.*, 2020, **10**, 39922

Facile sub-/supercritical water synthesis of nanoflake MoVTeNbO$_x$-mixed metal oxides without post-heat treatment and their catalytic performance

Shuangming Li,[ab] Yongwei Liu,[a] Yaoxin Fan,[a] Zixuan Lu,[a] Yunong Yan,[a] Luyao Deng,[a] Zhe Zhang[a] and Sansan Yu *[ab]

Received 10th August 2020
Accepted 19th October 2020

DOI: 10.1039/d0ra06877b

rsc.li/rsc-advances

A fast and simple sub-/supercritical water synthesis method is presented in this work in which MoVTeNbO$_x$-mixed metal oxides with various phase compositions and morphologies could be synthesized without post-heat treatment. It was demonstrated that the system temperature for synthesis had a significant influence on the physico-chemical properties of MoVTeNbO$_x$. Higher temperatures were beneficial for the formation of a mixed crystalline phase containing TeVO$_4$, Te$_3$Mo$_2$V$_2$O$_{17}$, Mo$_4$O$_{11}$ and TeO$_2$, which are very different from the crystalline phases of conventional Mo–V–Te–Nb-mixed metal oxides. While at lower temperatures, Mo$_4$O$_{11}$ was replaced by Te. At high temperature, the as-prepared samples presented distinct nanoflake morphologies with an average size of 10–60 nm in width and exhibited excellent catalytic performances in the selective oxidation of propylene to acrylic acid. It is illustrated that the large specific surface area, presence of Mo$_4$O$_{11}$ and superficial Mo^{6+} and Te^{4+} ions are responsible for the high propylene conversion, while suitable acidic sites and superficial Nb^{5+} ions improved the selectivity to acrylic acid.

1. Introduction

MoVTeNbO$_x$-mixed metal oxides are the most significant and promising catalysts for the selective oxidation of propylene/propane to acrylic acid. It is reported that the conversion of feed and selectivity to products is closely related to the chemical composition, structure and morphology of MoVTeNbO$_x$-mixed metal oxides, which depends greatly on the preparation methods.[1,2]

To date, MoVTeNbO$_x$-mixed oxides have been prepared by different synthesis routes, including slurry, co-precipitation, hydrothermal, dry-up and solid state reactions.[3-7] Among them, slurry and hydrothermal methods are the most common options; however, both of the processes need long reaction times that can take dozens of hours.[8-10] Furthermore, in order to improve the crystallinity and stability of products, a necessary post-heat treatment at 550–600 °C under a given atmosphere, lasting for several hours, is also involved in current routes. For instance, Ueda *et al.*[5] synthesized three Mo–V–O based oxides with single crystals by using a hydrothermal method at 175 °C for 48 h followed by calcination under nitrogen atmosphere for 2 h at 600 °C. Mazloom *et al.* prepared MoVTeNbO$_x$ using a slurry method, in which continuous evaporation at 60 °C was needed, firstly to remove the water in the precursor solution and a subsequent calcination at 600 °C for 2 h under nitrogen atmosphere was then carried out.[6] For the mixed oxides, most notably, these aforementioned complicated synthesis processes make complete reproduction difficult for other researchers. Therefore, it is urgent to develop a simple and fast route to prepare MoVTeNbO$_x$-mixed oxides.

Nowadays, sub-/supercritical water is widely used in the preparation of metal- and non-metal-based nano/micro materials, due to the unique and adjustable physicochemical properties around its critical point.[11-16] For instance, the low dielectric constant of sub-/supercritical water is conducive to the formation of nanoparticles of metal-based materials[17-23] and the hybridization of nanoparticles.[24] More importantly, under sub- and supercritical systems, the crystallization of metal-based products can be achieved in a very short time.[13,23-27] This makes the follow-up heat treatment of product no longer necessary, simplifying the preparation process greatly. Diez-Garcia *et al.* prepared highly crystalline fibrillar tobermorite in just a few seconds under supercritical water.[13] Lee *et al.* synthesized multivariate LiFePO$_4$ composite metal oxides by sub- and supercritical water in 1 h.[20] Zheng *et al.* synthesized pure-phase BaTeMo$_2$O$_9$ polycrystals in a supercritical water system.[28] Moreover, this technology can easily achieve scaled-up

---

[a] College of Chemical Engineering, Shenyang University of Chemical Technology, No. 9, 11 St., Shenyang Economic & Technological Development Zone, Shenyang 110142, China. E-mail: ssyu@syuct.edu.cn; Fax: +86 24 89383760; Tel: +86 24 89381190

[b] Key Laboratory of Chemical Separation Technology of Liaoning Province, Shenyang University of Chemical Technology, Shenyang 110142, China

production through continuous reaction with a simple flow type system. Nugroho and Hong *et al.* synthesized CoO_x, MnO_x and $Li_4Ti_5O_{12}$, $LiFePO_4$ nanoparticles by a continuous sub-/supercritical water process.[21,22,29-32] To the best of our knowledge, however, there is no report on the synthesis of $MoVTeNbO_x$-mixed metal oxides using sub- and supercritical water techniques at present.

Herein, a sub-/supercritical water technique is employed to fabricate $MoVTeNbO_x$-mixed metal oxides directly. A series of products are obtained by adjusting the synthesis system temperature within 1 h and without post-heat treatment. It is noteworthy that the products do not contain the M1/M2 crystalline phase, which exists in the traditional Mo–V–Te–Nb-mixed metal oxides. Moreover, it is very interesting that certain as-prepared products present distinctive nanoflake structures with large specific surface areas. Furthermore, the catalysis results reveal that the as-prepared products can catalyze the oxidation of propylene to acrylic acid efficiently with the maximum conversion of 89% and selectivity of 59%. It is demonstrated that sub-/supercritical water is a simple, rapid and promising method to synthesize efficient $MoVTeNbO_x$ catalysts.

2. Experimental section

2.1 Preparation

A $MoVTeNbO_x$-mixed oxide with a nominal Mo/V/Te/Nb atomic ratio of 1/0.31/0.37/0.065 was prepared by a sub-/supercritical water method. First, an aqueous solution containing $(NH_4)_6Mo_7O_{24}\cdot 4H_2O$ and NH_4VO_3 was prepared at room temperature. In parallel, TeO_2 and $Nb(HC_2O_4)_5\cdot xH_2O$ were dispersed/dissolved in deionized water, respectively. Next, the aqueous suspension of TeO_2 and $Nb(HC_2O_4)_5\cdot xH_2O$ solution was transferred into a Mo–V-mixed solution in sequence to form a light yellow slurry. The slurry was stirred at 80 °C for 1 h and then introduced into a SUS 316 tubular reactor with an inner volume of 10 mL. After being tightly sealed, the reactor was immersed into the molten salt bath (KNO_3, $NaNO_3$, and $Ca(NO_3)_2$ in the weight ratio of 46 : 24 : 30), which was heated to a desired temperature (250–450 °C) beforehand. After 1 h, the reactor was quenched in cold water. The resulting powders were filtered and washed with water several times. Then, the products were dried overnight at 90 °C under vacuum.

For the nomenclature, the final dark powder products obtained at 250, 300, 350, 400 and 450 °C were labeled as S250, S300, S350, S400 and S450, respectively. All of the above reagents were analytical reagent (AR) grade and purchased from Sinopharm Chemical Reagent Co, Ltd. (Shanghai, China).

2.2 Characterization

The powder X-ray diffraction (XRD) patterns were recorded on an Empyrean X-ray generator (PANalytical B.V., Netherlands). Diffraction intensities were measured from 20 to 50° with a 2θ step of 0.01° for 8 s per point using Cu Kα radiation. The transmission electron microscopy (TEM) and energy dispersive X-ray spectroscopy (EDX) were carried out by using a TECNAI G2 F20 microscope (FEI, USA) equipped with an EDX analyzer system at an accelerating voltage of 200 kV. The X-ray photoelectron spectroscopy (XPS) was carried out on an ESCALAB250 spectrometer (Thermo Electron, USA). Hydrogen temperature-programmed reduction (H_2-TPR) and ammonia temperature-programmed desorption (NH_3-TPD) were carried out in a ChemBET system (Quantachrome, USA) equipped with a thermal conductivity detector. For H_2-TPR, 0.1 g catalyst was reduced in 10% H_2/Ar with a flow rate of 30 mL min^{-1} from room temperature to 800 °C at a heating rate of 10 °C min^{-1}. For NH_3-TPD, catalysts were carried out in 7% NH_3/He from room temperature to 700 °C with the same heating rate. The specific surface area was recorded by the BET method using nitrogen adsorption–desorption isotherms at liquid nitrogen temperature of −196 °C on an Autosorb-IQ gas adsorption analyzer (Quantachrome, America).

2.3 Catalytic tests

The catalytic performance of $MoVTeNbO_x$-mixed oxides was evaluated under different temperatures ranging from 380 to 440 °C at atmospheric pressure. The experiments were carried out in a fixed-bed stainless steel tubular reactor (i.d. 8 mm; length 400 mm). After being tableted, crushed and sieved, 1.0 g of each catalyst was diluted with silica sands of the same quality in order to achieve homogeneous heat distribution within the catalyst bed, and then introduced in the middle of the reactor. Afterward, the reactor was heated to the desired temperature under the reaction gas feed flow composed of C_3H_6, H_2O, N_2 and O_2 in the mole ratio of 1.0 : 3.0 : 8.0 : 1.8. The reaction products were collected at a given time interval after being condensed with ice water and then analyzed by a gas chromatograph (GC7890, Agilent, USA) equipped with a thermal conductivity detector (TCD) and Porapak-Q column.

3. Results and discussion

3.1 Characterization

Fig. 1 shows the XRD patterns of as-prepared $MoVTeNbO_x$-mixed oxide samples under different temperatures in a sub-/supercritical water system. For S250 and S300, the diffraction peaks are indexed to mixed phases of $TeVO_4$, $Te_3Mo_2V_2O_{17}$,

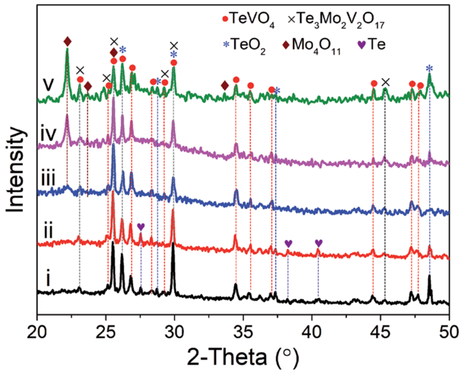

Fig. 1 XRD patterns of $MoVTeNbO_x$ samples. S250 (i), S300 (ii), S350 (iii), S400 (iv) and S450 (v).

TeO_2 and Te. These main peaks at $2\theta = 23.0, 25.5, 26.1, 26.8, 29.8, 34.4, 44.4$ and $47.2°$ are related to $TeVO_4$ (JCPDS # 25-0930), the peaks located at $2\theta = 23.0, 25.5, 26.1, 29.8$, and $45.4°$ are attributable to $Te_3Mo_2V_2O_{17}$ (JCPDS # 35-0129), the peaks at $2\theta = 26.1, 29.8, 37.3$ and $48.5°$ are associated with TeO_2 (JCPDS # 74-1666) and the peaks at 27.5, 38.2 and 40.4° correspond to Te (JCPDS # 36-1452). For S350, another phase ($2\theta = 22.1, 23.6$ and $25.5°$) corresponding to orthorhombic Mo_4O_{11} (JCPDS # 65-2473) emerges in the pattern. Moreover, it is apparent that the relative peak intensity of Mo_4O_{11} increases obviously when the temperature was elevated from 350 to 450 °C (see pattern iv and v). In contrast, the peaks belonging to Te become very weak from pattern iii to v.

It is clear that the sub-/supercritical water system temperature had a substantial influence on the crystal phase composition of $MoVTeNbO_x$-mixed oxides. Four phases including $TeVO_4$, $Te_3Mo_2V_2O_{17}$, Te and Mo_4O_{11} could be synthesized, in which the former two were the essential constituents, while Te and Mo_4O_{11} were formed only under certain conditions. Higher temperatures were favorable for the fabrication of Mo_4O_{11}, whereas the formation of Te occurred at lower temperatures. It should be noted that the diffraction peaks of TeO_2 existed in all samples, suggesting some tellurium dioxide did not participate in the reaction, but the morphology changed in the process. Moreover, Mo_4O_{11} was an oxygen defect shear structure of MoO_3.[33] Based on this, it was possible that MoO_3 was first formed *via* the decomposition of $(NH_4)_6Mo_7O_{24}\cdot 4H_2O$ and then further converted to Mo_4O_{11} through phase evolution under the sub-/supercritical water system with a rapid heating and quenching process.[34] No phase formed by Nb was observed, which is probably due to the insertion of Nb into the lattice of other mixed oxide systems ($TeVO_4$ and $Te_3Mo_2V_2O_{17}$) as a substitution element for V.[35] The above results reveal that $MoVTeNbO_x$-mixed oxides with different crystal phase compositions can be facilely and controllably fabricated by adjusting the synthesis system temperature.

Fig. 2 and 3 show the TEM and HRTEM images and EDX analyses of as-synthesized $MoVTeNbO_x$-mixed oxides at different synthesis system temperatures. As shown in Fig. 2, S250 and S300 present obvious assembled morphologies that form aggregates of small particles (Fig. 2a–c), whereas S350, S400 and S450 display distinct nanoflake-like morphologies (Fig. 3a–c). On the one hand, such a morphology change of $MoVTeNbO_x$ can be explained by the crystal re-growth resulting from the improved solubility of products at the higher temperature. Small crystalline nuclei were first formed in a supersaturated solution and then followed by subsequent crystal growth, which is just like the Ostwald ripening process.[36,37] On the other hand, according to the XRD patterns in Fig. 1, orthorhombic Mo_4O_{11} arose when the preparation temperature increased from 300 to 350 °C. It was documented that the orthorhombic crystal system is inclined to anisotropic growth and easily forms flakes.[38] Therefore, the existence of orthorhombic Mo_4O_{11} in these samples might be another reason for the change of morphology. Furthermore, it is noteworthy that with the increase of synthesis system temperature, the dimension of these flakes evolves gradually from slender (average size of 10 nm in width and 200 nm in length for S350) (Fig. 3a) to short and thick (average size of 60 nm in width and 100 nm in length for S450) (Fig. 3c). According to crystal growth theory, the crystal morphology is usually determined by the relative growth rate of the different crystal faces.[39] Therefore, it was inferred that the surface energy of each crystal face of the product was different under the given sub-/supercritical water system, leading to various growth rates between crystal faces. Consequently, nanoflakes with different widths and lengths were formed along with the elimination of fast growing crystal facets and the preservation of slow ones. EDX analyses in Fig. 2b and c and 3a–c further indicate the presence of Mo, V, Te and Nb in $MoVTeNbO_x$ samples. Moreover, the detailed HRTEM characterizations show that various interplanar spacing d values are observed in S350–S450 (Fig. 3d–i), among which 0.352, 0.333 and 0.337 nm can be attributed to the (-111), (-112) and (102) lattice planes of $TeVO_4$, 0.406 nm corresponds to the (101) lattice plane of TeO_2 or (600) of Mo_4O_{11}, while 0.397, 0.398, 0.400, and 0.336 nm are assigned to the (211) and (002) lattice planes of Mo_4O_{11}, respectively.

XPS was applied to investigate the element valence state on the sample surface. Fig. 4 presents the XPS survey spectrum and

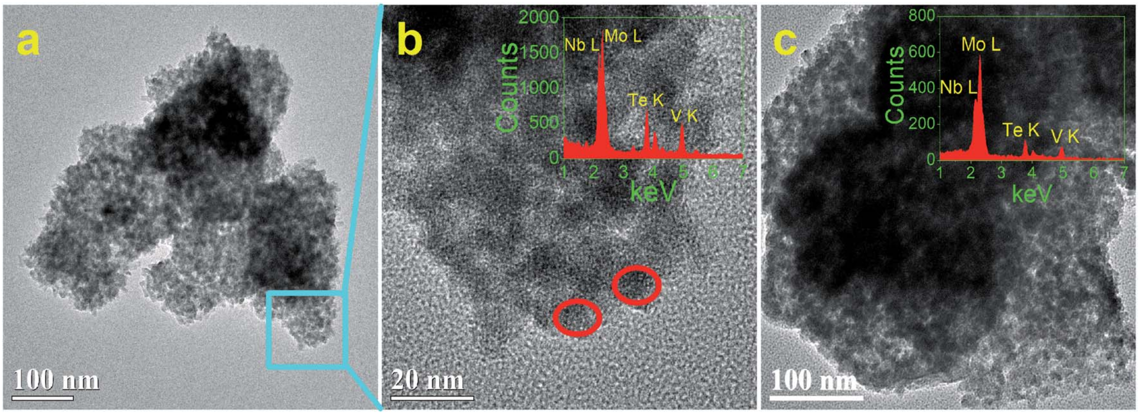

Fig. 2 TEM, HRTEM images and EDX analyses of $MoVTeNbO_x$ samples, S250 (a and b) and S300 (c). ((b) is the detailed morphology of the zone marked in (a), and the insets are the corresponding EDX).

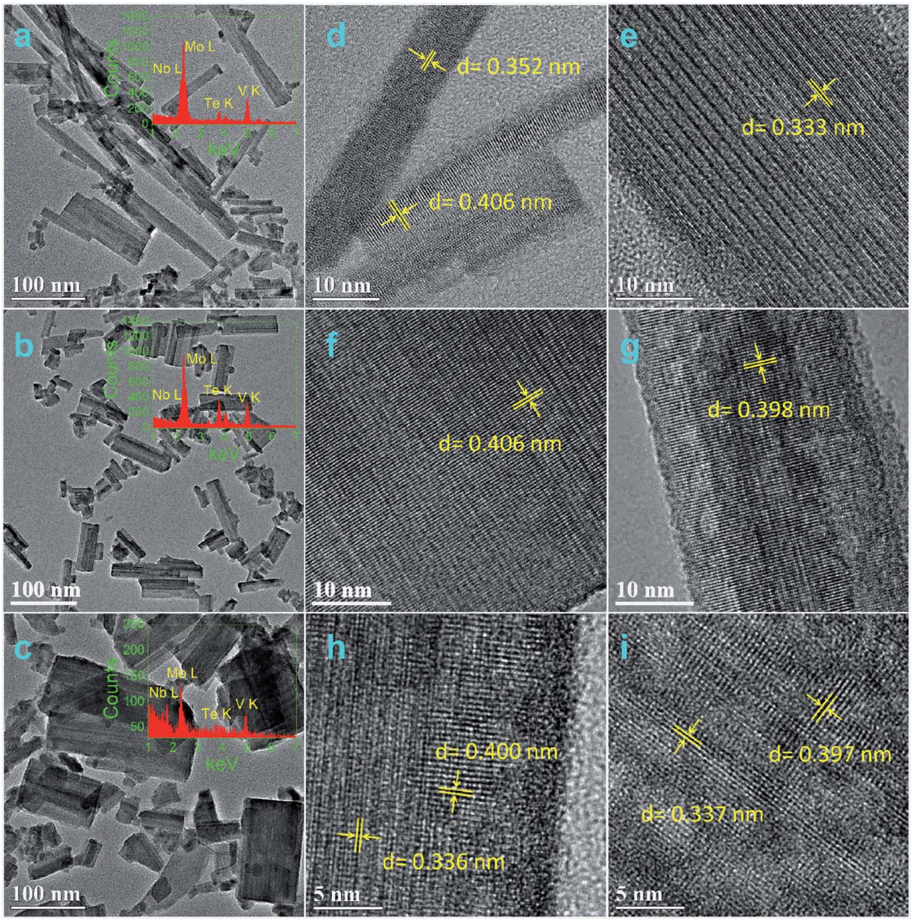

Fig. 3 TEM, HRTEM images and EDX analyses of MoVTeNbO$_x$ samples, S350 (a, d, e), S400 (b, f, g), and S450 (c, h, i) (the insets are the corresponding EDX).

high resolution spectra of Mo 3d, V 2p, Te 3d, Nb 3d and O 1s of MoVTeNbO$_x$, in which XPS spectra were calibrated to the adventitious C 1s peak at a binding energy of 284.6 eV. In the XPS survey spectra (Fig. 4a), five peaks centered at around 232.8, 516.0, 575.9, 207.1 and 530.0 eV correspond to Mo 3d$_{5/2}$, V 2p$_{3/2}$, Te 3d$_{5/2}$, Nb 3d$_{5/2}$ and O 1s, respectively.[40–44] Fig. 4b shows that the Mo 3d$_{5/2}$ BE peak of S250 can be split into two peaks at 232.8 and 232.0 eV, indicating that the surface Mo species consist of Mo^{6+} and Mo^{5+}.[45,46] For S300 and S350, there are also both Mo^{6+} and Mo^{5+}. However, considering that the peak values are closer to 232.8 eV, the amount of Mo^{6+} largely outweighs that of Mo^{5+}. Split peak fitting further verifies this. On the surface of S400 and S450, only Mo^{6+} is detected, illustrating that higher synthesis temperatures are favorable for the enrichment of Mo^{6+} on the sample surface. For V, two valence states of +4 (516.0 eV) and +5 (517.0 eV)[43,46] exist on the surface of all MoVTeNbO$_x$ samples (Fig. 4c), and it is clear that V^{4+} has the highest concentration. In Fig. 4d, the BE value around 575.9 eV (Te 3d$_{5/2}$) can be attributed to Te^{4+},[42,,47,48] demonstrating tellurium is in a uniform state on the sample surfaces. As Fig. 4e shown, the Nb 3d peak of S250 is split into two peaks at 206.3 and 207.1 eV, which are ascribed to Nb^{4+} and Nb^{5+}, respectively.[48–50] Unlike S250, only Nb^{5+} exists in the samples of S300–S450. It can be seen from Fig. 4b and e that more low valence metal ions such as Mo^{5+} and Nb^{4+} exist on the surface of S250 than that of S300–S450, which is probably due to the weaker oxidation of subcritical water at low temperatures. Furthermore, the peaks of O 1s can be fit into two peaks centered at binding energies of 530.0 and 531.1 eV, which belong to the typical metal–oxygen bonding and lattice oxygen, respectively.[44,51]

The acid sites of as-synthesized samples were determined by NH$_3$-TPD and the profiles are presented in Fig. 5a. According to the literature, the desorption peaks centered at 250 °C and 624 °C in the profile of sample S250, marked as α and β, can be attributed to weak and strong acidic sites, respectively.[52,53] With the increase of synthesis temperature from 250 to 400 °C, the area of peak α is continuously enlarged, meanwhile, an obvious shift of peak β to higher temperatures (from 624 °C for S250 to 710 °C for S450) is observed. In addition, another desorption peak γ, also corresponding to strong acidic sites, emerges at 577 °C in the curve of S400, which is enlarged greatly in S450. Unlike the former four samples, S450 possesses peak δ (326 °C) related to medium acidic sites[52,53] instead of peak α. According to the results of XRD and XPS, it could be seen that the amount of the Mo$_4$O$_{11}$ phase, Mo^{6+} and Nb^{5+} increased evidently with the increase of synthesis system temperature. It was reported

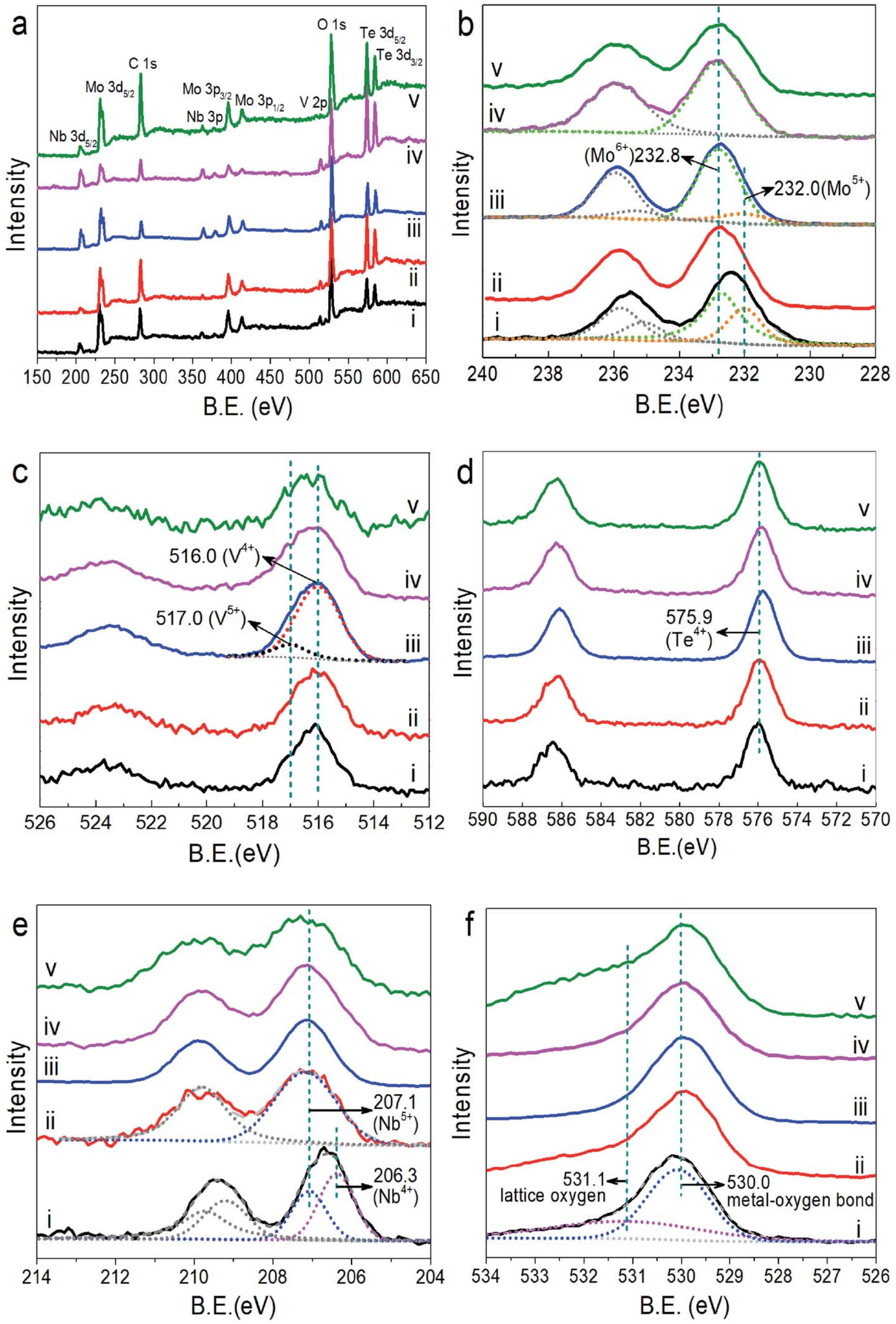

Fig. 4 XPS full survey spectra (a), high resolution spectra XPS spectra of Mo 3d (b), V 2p (c), Te 3d (d), Nb 3d (e) and O 1s (f) of MoVTeNbO$_x$. S250 (i), S300 (ii), S350 (iii), S400 (iv) and S450 (v).

that metallic oxides with high valence states could behave as acidic oxides.[33] Therefore, the increase of Mo^{6+}, Nb^{5+} and the corresponding phase could be responsible for the shift of acid sites to high temperature and abundance.

The reduction behaviors of MoVTeNbO$_x$ are examined by H$_2$-TPR. As Fig. 5b shows, six types of reduction peaks at 495 (I), 533–549 (II), 586–633 (III), 660–693 (IV), 703–733 (V) and 728 °C (VI) are observed in the H$_2$-TPR profiles of samples. It is documented that the peak type I, II and III at low temperature originate from the reduction of metal cation (Mo^{6+}, V^{5+} and Te^{4+}) species in mixed metal oxides[54–57] while type IV can be attributed to the reduction of TeMoO$_x$.[58] Moreover, the peak type V and VI at high temperatures are likely related to the monometallic oxide. According to the study, the reduction temperature can reflect the migration of lattice oxygen from the bulk to the surface.[57] Therefore, the S250 sample exhibited the greatest reducibility of lattice oxygen. In addition, these samples display changes in the TPR patterns depending on the synthesis system temperature and there is an obvious tendency for reduction peaks to move towards high temperatures from

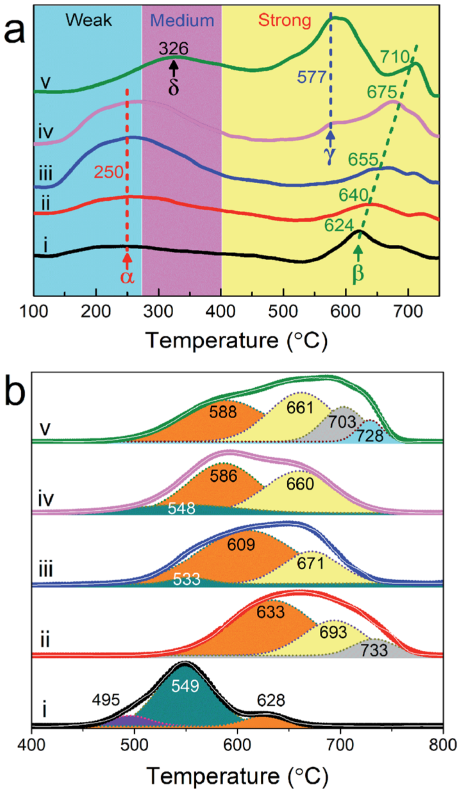

Fig. 5 NH_3-TPD (a) and H_2-TPR (b) profiles of $MoVTeNbO_x$. S250 (i), S300 (ii), S350 (iii), S400 (iv) and S450 (v).

S250 to S450. The total peak areas of S300, S350, S400 and S450 are larger than that of S250, indicating that the number of lattice oxygens in samples increased dramatically[59] when the synthesis system temperature was higher than 250 °C.

The N_2 adsorption–desorption isotherms and specific surface area of the samples are shown in Fig. 6. The isotherm profiles of all the samples exhibit a type III isotherm based on the IUPAC classification, featuring an H3-type hysteresis loop in the relative pressure (P/P^0) of 0.2–1.0 (Fig. 6a). In addition, with the increase of synthesis system temperature, the specific surface area of samples is increased progressively. As shown in Fig. 6b, S250 shows the lowest specific surface area of 10.93 m^2 g^{-1}, while S450 as-prepared at the highest temperature possesses the maximal specific surface area of 66.52 m^2 g^{-1}. S300, S350 and S400 exhibit that of 18.49, 28.27 and 62.39 m^2 g^{-1}, respectively. In view of the close relationship between the specific surface area and morphology, it was supposed that the low specific surface areas of S250 and S300 could be ascribed to the agglomeration of particles.

3.2 Catalytic performance

The catalytic performance of as-prepared $MoVTeNbO_x$ was tested for the selective oxidation of propylene to acrylic acid at different catalytic temperatures with an interval of 20 °C (380, 400, 420 and 440 °C) and the results are shown in Fig. 7. It can be observed that there is an apparent rising trend in propylene conversion with the increase of synthesis system temperature (from S250 to S450) for all catalytic temperatures (see line chart in Fig. 7), and the conversion reaches a maximum of 89% at 420 °C for sample S450 (Fig. 7c). Furthermore, the selectivity to acrylic acid ranges from 22.07% to 54.16%, in which sample S250 and S300 exhibit the minimum and maximum at catalytic temperatures of 400 °C and 440 °C, respectively. It is apparent that the catalytic temperature had a great influence on the selectivity to acrylic acid, and almost all samples exhibit the maximum selectivity at 400 °C.

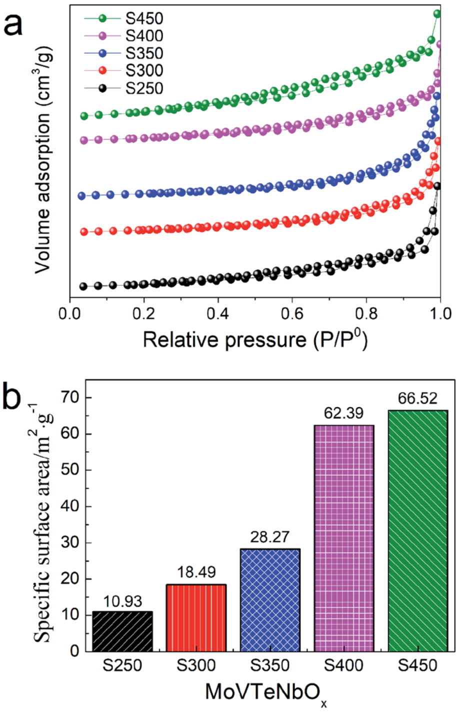

Fig. 6 N_2 adsorption–desorption isotherms (a) and the BET specific surface areas (b) of $MoVTeNbO_x$.

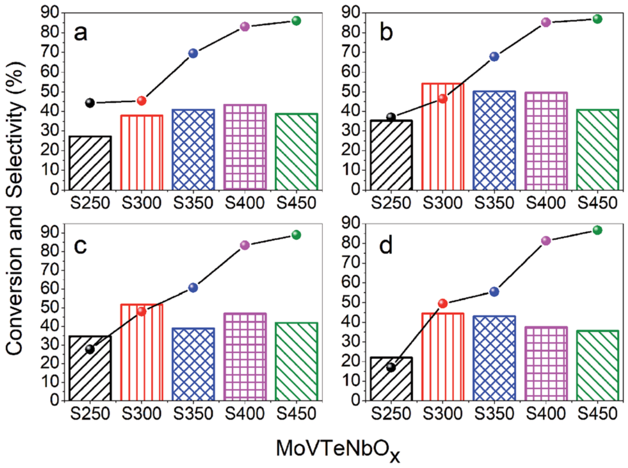

Fig. 7 The catalytic performance of $MoVTeNbO_x$ for selective oxidation of propylene to acrylic acid at test temperatures of 380 (a), 400 (b), 420 (c) and 440 °C (d), respectively. Line and column charts correspond to the conversion of propylene and selectivity to acrylic acid, respectively.

It is well known that the activity of a catalyst is greatly affected by the specific surface area. In this work, the trend of propylene conversion was completely consistent with that of the specific surface area of samples (Fig. 6b and 7). S450 possessed the largest specific surface area, which is one of the main reasons for its maximum propylene conversion. In addition, S450 and S400 contained more of the Mo_4O_{11} phase (Fig. 1), an oxygen defect shear structure of MoO_3, which has shown excellent catalytic activity for the oxidation of propylene.[33,60] The XPS results showed that there were abundant superficial Mo^{6+} ions in the samples, which also played an important role in such a reaction. On the one hand, Mo^{6+} could strengthen the binding of the catalyst with the organic fragment, facilitating the hydrolysis reaction of this surface complex on its path towards acrylic acid formation.[61] On the other, the synergism of Mo^{6+} and Te^{4+} could abstract an allylic hydrogen from propylene, improving the conversion of propylene.[62] For the same reason, the lowest ratio of Mo^{6+}/Mo^{5+} of S250 might be another reason for its lowest propylene conversion. Although S250 possessed the greatest reducibility of lattice oxygen (Fig. 5b), it did not seem to play a significant role in activating propylene.

Compared with the other four catalysts, S250 showed the worst selectivity to acrylic acid at all catalytic temperatures, which might be attributed to the less weak acidic sites and more strong acidic sites (see Fig. 5a). It is documented that the superficial acid–base properties of a catalyst have an important effect on the selectivity of partial oxidation reactions.[8,46] The ideal acidity of the catalyst should be able to interact properly with the reactant and target product to facilitate desorption of target products, avoiding over-oxidation. Besides S250, the average selectivity of S450 was also significantly lower than that of S300, S350 and S400, which was ascribed to the over-oxidation caused by the more strong acidic sites. In addition, Nb was also considered to improve the selectivity to acrylic acid by reducing the over-oxidation rate of acrylic acid.[5,35] Based on this, it was speculated that the more superficial niobium ions with low valence states of S250 (Fig. 4e) had an adverse impact on its selectivity.

Time-on-stream experiments were also carried out to investigate the stability of the prepared catalyst. Taking S400 catalyst as an example, the time-on-stream results of selective oxidation of propylene to acrylic acid over $MoVTeNbO_x$ at 400 °C are shown in Fig. 8. It is revealed that the conversion of propylene and selectivity to acrylic acid is well-maintained during a 30 h reaction test.

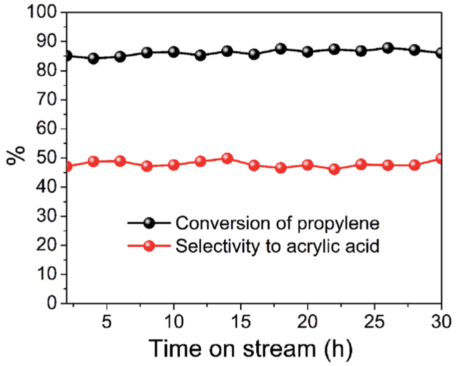

Fig. 8 Time-on-stream of selective oxidation of propylene to acrylic acid over $MoVTeNbO_x$ (S400 catalyst) at 400 °C.

In addition, the structure and performance of the catalysts in this work were compared with the $MoVTeNbO_x$-mixed metal oxides prepared conventionally. It was documented that the most important factor affecting the performance of $MoVTeNbO_x$ catalyst is the phase composition. The phases of conventional $MoVTeNbO_x$ catalysts for propylene oxidation to acrylic acid consist of M1, M2, $Mo_{5-x}(V/Nb)_xO_{14}$, $V_{0.95}Mo_{0.97}O_x$, $TeMo_5O_{16}$, $TeMo_4O_{13}$ and $V_{0.33}Mo_{0.67}O_2$. It was reported that the conversion of propylene and selectivity to acrylic acid range from 4.5–86.9% and 0–89.6%, respectively.[7,61,63,64] Among which, the highest yield of 56.1% could be obtained when the crystal phase of the catalyst was pure M1.[63] In this work, distinct phases consisting of $TeVO_4$, $Te_3Mo_2V_2O_{17}$, Mo_4O_{11} and TeO_2 were detected. Nevertheless, the results showed that these catalysts also exhibit good performance, in which the highest conversion and selectivity achieved 88.9% and 54.2%, respectively.

4. Conclusions

Five $MoVTeNbO_x$-mixed metal oxides were fabricated simply and rapidly by using a sub-/supercritical water technique without a post-heat treatment and their catalytic performance were investigated. It is concluded that the crystalline phase, morphology, surface properties, as well as acidic and redox properties were influenced greatly by the synthesis system temperature. Nanoflake-like $MoVTeNbO_x$ consisting of $TeVO_4$, $Te_3Mo_2V_2O_{17}$, Mo_4O_{11} and TeO_2 were obtained at 400–450 °C, showing large specific surface areas of *ca.* 62–66 $m^2\ g^{-1}$. Compared with the others, the samples prepared at 250 °C possessed more superficial Mo^{5+} and Nb^{4+}. In the process of catalytic reaction, there was a significant positive correlation between the conversion of propylene and the specific surface area of the samples. A certain amount of Mo_4O_{11} and superficial Mo^{6+}, Te^{4+} ions also contributed to the conversion. Samples prepared at 300–400 °C owning suitable acidic sites and adequate superficial Nb^{5+} ions showed excellent selectivity to acrylic acid, in which the maximum yield of acrylic acid reached 43%. For the synthesis of a $MoVTeNbO_x$ catalyst with excellent catalytic performance, it is demonstrated that sub-/supercritical water is a simple, rapid and promising method.

Conflicts of interest

There are no conflicts of interest to declare.

Acknowledgements

The authors gratefully acknowledge the financial supports by the National Natural Science Foundation of China (Grant No. 21706165), Scientific Research Fund of Liaoning Provincial Education Department, China (Grant No. LQ2019007) and the Natural Science Foundation of Liaoning Province, China (Grant No. 20170540714).

References

1. J. S. Valente, H. Armendáriz-Herrera, R. Quintana-Solórzano, P. del Ángel, N. Nava, A. Massó and J. M. López Nieto, *ACS Catal.*, 2014, **4**, 1292–1301.
2. E. V. Ishchenko, T. V. Andrushkevich, G. Y. Popova, T. Y. Kardash, A. V. Ishchenko, L. S. Dovlitova and Y. A. Chesalov, *Appl. Catal., A*, 2014, **476**, 91–102.
3. H. Watanabe and Y. Koyasu, *Appl. Catal., A*, 2000, **194–195**, 479–485.
4. H. Jiang, W. Lu and H. Wan, *Catal. Commun.*, 2004, **5**, 29–34.
5. W. Ueda, D. Vitry and T. Katou, *Catal. Today*, 2005, **99**, 43–49.
6. G. Mazloom and S. M. Alavi, *Part. Sci. Technol.*, 2014, **33**, 204–212.
7. D. Vitry, Y. Morikawa, J. L. Dubois and W. Ueda, *Appl. Catal., A*, 2003, **251**, 411–424.
8. S. Hernández-Morejudo, A. Massó, E. García-González, P. Concepción and J. M. López Nieto, *Appl. Catal., A*, 2015, **504**, 51–61.
9. L. Annamalai, Y. Liu, S. Ezenwa, Y. Dang, S. L. Suib and P. Deshlahra, *ACS Catal.*, 2018, **8**, 7051–7067.
10. A. L. Pacquette, D. S. Oh and A. A. Gewirth, *J. Phys. Chem. C*, 2016, **120**, 15553–15562.
11. M. Claverie, M. Diez-Garcia, F. Martin and C. Aymonier, *Chemistry*, 2019, **25**, 5814–5823.
12. H. Weingartner and E. U. Franck, *Angew. Chem.*, 2005, **44**, 2672–2692.
13. M. Diez-Garcia, J. J. Gaitero, J. S. Dolado and C. Aymonier, *Angew. Chem., Int. Ed. Engl.*, 2017, **56**, 3162–3167.
14. C. Aymonier, G. Philippot, A. Erriguible and S. Marre, *J. Supercrit. Fluids*, 2018, **134**, 184–196.
15. S. P. Sasikala, P. Poulin and C. Aymonier, *Adv. Mater.*, 2017, **29**, 1605473.
16. T. Voisin, A. Erriguible, D. Ballenghien, D. Mateos, A. Kunegel, F. Cansell and C. Aymonier, *J. Supercrit. Fluids*, 2017, **120**, 18–31.
17. L. Maurizi, F. Bouyer, M. Ariane, R. Chassagnon and N. Millot, *RSC Adv.*, 2014, **4**, 45673–45678.
18. A. Aimable, H. Muhr, C. Gentric, F. Bernard, F. Le Cras and D. Aymes, *Powder Technol.*, 2009, **190**, 99–106.
19. B. Jiang, C. Li, M. Imura, J. Tang and Y. Yamauchi, *Adv. Sci.*, 2015, **2**, 1500112.
20. J. Lee and A. S. Teja, *Mater. Lett.*, 2006, **60**, 2105–2109.
21. A. Nugroho, D. Yoon, O.-S. Joo, K. Y. Chung and J. Kim, *Chem. Eng. J.*, 2014, **258**, 357–366.
22. A. Nugroho and J. Kim, *J. Ind. Eng. Chem.*, 2014, **20**, 4443–4446.
23. M. Diez-Garcia, J. J. Gaitero, J. I. Santos, J. S. Dolado and C. Aymonier, *J. Flow Chem.*, 2018, **8**, 89–95.
24. H. Hayashi and Y. Hakuta, *Materials*, 2010, **3**, 3794–3817.
25. T. Adschiri, Y. Hakuta and K. Arai, *Ind. Eng. Chem. Res.*, 2000, **39**, 4901–4907.
26. Y. Hakuta, H. Hayashi and K. Arai, *Curr. Opin. Solid State Mater. Sci.*, 2003, **7**, 341–351.
27. R. B. Yahya, H. Hayashi, T. Nagase, T. Ebina, Y. Onodera and N. Saitoh, *Chem. Mater.*, 2001, **13**, 842–847.
28. Q. Zheng, B. Li and X. Tao, *CrystEngComm*, 2011, **13**, 750–752.
29. S.-A. Hong, S. J. Kim, K. Y. Chung, Y.-W. Lee, J. Kim and B.-I. Sang, *Chem. Eng. J.*, 2013, **229**, 313–323.
30. S.-A. Hong, S. J. Kim, K. Y. Chung, M.-S. Chun, B. G. Lee and J. Kim, *J. Supercrit. Fluids*, 2013, **73**, 70–79.
31. S.-A. Hong, S. J. Kim, J. Kim, B. G. Lee, K. Y. Chung and Y.-W. Lee, *Chem. Eng. J.*, 2012, **198–199**, 318–326.
32. A. Nugroho, S. J. Kim, K. Y. Chung, B.-W. Cho, Y.-W. Lee and J. Kim, *Electrochem. Commun.*, 2011, **13**, 650–653.
33. J. C. Védrine, E. K. Novakova and E. G. Derouane, *Catal. Today*, 2003, **81**, 247–262.
34. M. Mihalev, C. Hardalov, C. Christov, M. Michailov, B. Ranguelov and H. Leiste, *J. Phys.: Conf. Ser.*, 2014, **514**, 012022.
35. W. Ueda, D. Vitry and T. Katou, *Catal. Today*, 2004, **96**, 235–240.
36. S. Sun, P. Li, S. Liang and Z. Yang, *Nanoscale*, 2017, **9**, 11357–11404.
37. C. Coughlan, M. Ibanez, O. Dobrozhan, A. Singh, A. Cabot and K. M. Ryan, *Chem. Rev.*, 2017, **117**, 5865–6109.
38. G. Tan, J. Huang, L. Zhang, H. Ren and A. Xia, *Ceram. Int.*, 2014, **40**, 11671–11679.
39. J. B. Rawlings, S. M. Miller and W. R. Witkowski, *Ind. Eng. Chem. Res.*, 1993, **32**, 1275–1296.
40. E. V. Ishchenko, R. V. Gulyaev, T. Y. Kardash, A. V. Ishchenko, E. Y. Gerasimov, V. I. Sobolev and V. M. Bondareva, *Appl. Catal., A*, 2017, **534**, 58–69.
41. R. López-Medina, M. O. Guerrero-Pérez and M. A. Bañares, *New J. Chem.*, 2019, **43**, 17661–17669.
42. T. Y. Kardash, E. V. Lazareva, D. A. Svintsitskiy, E. P. Kovalev and V. M. Bondareva, *Kinet. Catal.*, 2019, **60**, 355–365.
43. Y. S. Yun, M. Lee, J. Sung, D. Yun, T. Y. Kim, H. Park, K. R. Lee, C. K. Song, Y. Kim, J. Lee, Y.-J. Seo, I. K. Song and J. Yi, *Appl. Catal., B*, 2018, **237**, 554–562.
44. H. W. Nam, C. V. V. M. Gopi, S. Sambasivam, R. Vinodh, K. V. G. Raghavendra, H.-J. Kim, I. M. Obaidat and S. Kim, *J. Energy Storage*, 2020, **27**, 101055.
45. K. Asakura, K. Nakatani, T. Kubota and Y. Iwasawa, *J. Catal.*, 2000, **194**, 309–317.
46. E. V. Ishchenko, T. Y. Kardash, R. V. Gulyaev, A. V. Ishchenko, V. I. Sobolev and V. M. Bondareva, *Appl. Catal., A*, 2016, **514**, 1–13.
47. X. Yang, R. Feng, W. Ji and C. Au, *J. Catal.*, 2008, **253**, 57–65.
48. G. Wang, Y. Guo and G. Lu, *Fuel Process. Technol.*, 2015, **130**, 71–77.
49. G. Mestl, J. L. Margitfalvi, L. Végvári, G. P. Szijjártó and A. Tompos, *Appl. Catal., A*, 2014, **474**, 3–9.
50. M. K. Bahl, *J. Phys. Chem. Solids*, 1975, **36**, 485–491.
51. M. Hua, L. Xu, F. Cui, J. Lian, Y. Huang, J. Bao, J. Qiu, Y. Xu, H. Xu, Y. Zhao and H. Li, *J. Mater. Sci.*, 2018, **53**, 7621–7636.
52. N. Karanwal, D. Verma, P. Butolia, S. M. Kim and J. Kim, *Green Chem.*, 2020, **22**, 766–787.
53. V. Ranaware, D. Verma, R. Insyani, A. Riaz, S. M. Kim and J. Kim, *Green Chem.*, 2019, **21**, 1021–1042.
54. B. Chu, H. An, X. Chen and Y. Cheng, *Appl. Catal., A*, 2016, **524**, 56–65.

55 R.-M. Feng, X.-J. Yang, W.-J. Ji, H.-Y. Zhu, X.-D. Gu, Y. Chen, S. Han and H. Hibst, *J. Mol. Catal. A: Chem.*, 2007, **267**, 245–254.
56 X.-J. Yang, R.-M. Feng, W.-J. Ji and C.-T. Au, *J. Catal.*, 2008, **253**, 57–65.
57 Z. Deng, H. Wang, W. Chu and W. Yang, *Chin. J. Catal.*, 2008, **29**, 1032–1036.
58 I. Ramli, P. Botella, F. Ivars, W. Pei Meng, S. M. M. Zawawi, H. A. Ahangar, S. Hernández and J. M. L. Nieto, *J. Mol. Catal. A: Chem.*, 2011, **342–343**, 50–57.
59 H. Wang, Z. Deng, W. Chu and W. Yang, *Chin. J. Catal.*, 2009, **30**, 490–496.
60 T. V. Andrushkevich, L. M. Plyasova, G. G. Kuznetsova, V. M. Bondareva, T. P. Gorshkova, I. P. Olenkova and N. I. Lebedeva, *React. Kinet. Catal. Lett.*, 1979, **12**, 463–467.
61 R. K. Grasselli, C. G. Lugmair, A. F. Volpe, A. Andersson and J. D. Burrington, *Catal. Lett.*, 2008, **126**, 231–240.
62 R. K. Grasselli, *Catal. Today*, 2005, **99**, 23–31.
63 F. Ivars, B. Solsona, S. Hernández and J. M. López Nieto, *Catal. Today*, 2010, **149**, 260–266.
64 R. K. Grasselli, C. G. Lugmair, A. F. Volpe Jr, A. Andersson and J. D. Burrington, *Catal. Today*, 2010, **157**, 33–38.